LA-UR 11-03057

Quarter-wave pulse tube

G. W. Swift, D. L. Gardner, and S. Backhaus

Condensed Matter and Magnet Science Group,

Los Alamos National Laboratory,

Los Alamos, New Mexico 87545

(Dated: August 8, 2011)

Abstract

In high-power pulse-tube refrigerators, the pulse tube itself can be very long without too much dissipation of acoustic power on its walls. The pressure amplitude, the volume-flow-rate amplitude, and the time phase between them evolve significantly along a pulse tube that is about a quarter-wavelength long. Proper choice of length and area makes the oscillations at the ambient end of the long pulse tube optimal for driving a second, smaller pulse-tube refrigerator, thereby utilizing the acoustic power that would typically have been dissipated in the first pulse-tube refrigerator's orifice. Experiments show that little heat is carried from the ambient heat exchanger to the cold heat exchanger in such a long pulse tube, even though the oscillations are turbulent and even when the tube is compactly coiled.

Keywords: Pulse-tube refrigerator, quarter-wave pulse tube

Corresponding author: Greg Swift, swift@LANL.gov, 505-665-0640

I. INTRODUCTION

Cryogenic Stirling and pulse-tube refrigerators rely on identical gas-cycle thermodynamics in their regenerators and heat exchangers.[1] The Stirling refrigerator is more efficient because its cold piston or displacer recovers acoustic power from the gas near the cold heat exchanger, while the pulse-tube refrigerator (PTR) is mechanically simpler because it has no cold moving parts.

In a PTR, the pulse tube itself holds an oscillating, thermally stratified column of gas that would, under ideal circumstances, carry no heat from ambient to cryogenic temperature while transmitting acoustic power from cryogenic to ambient temperature without loss. In orifice PTRs, the transmitted acoustic power is dissipated in the resistance of an impedance network at the ambient end of the pulse tube, as shown in Fig. 1(a). Using the vocabulary of lumped-element acoustics,[2] the impedance network usually consists of a resistance, an inertance, and a compliance in series. These components can often be designed to optimize the performance of the regenerator, most easily for cooling powers above tens of watts. For example, part of the inertance can cancel the compliance in the pulse tube, cold heat exchanger, and cold part of the regenerator, thereby setting the time phases of oscillating pressure and velocity equal somewhere in the regenerator. This minimizes the amplitude of the velocity in the regenerator, and attendant viscous losses.

Although the gas in a pulse tube of typical length is usually thought of as purely compliant, its own inertance can be important at high enough frequency. The inertial impedance of a short column of gas of length Δx and cross-sectional area A is approximately $i\omega\rho\ \Delta x/A$, where ω is the radian frequency of the oscillation, ρ is the mean density of the gas, and $i = \sqrt{-1}$. The 350-Hz PTR of Godshalk et al.[3] demonstrated very good regenerator time-phase optimization using the pulse-tube's inertance to cancel its own compliance as well as that of other components.

In this paper, we explore the behavior of a much longer pulse tube in which both inertial and compliant effects are important and oscillating pressure p_1 and oscillating volume flow rate U_1 evolve significantly: a quarter-wavelength-long pulse tube. At the high cooling powers needed for energy-intensive cryogenic applications such as natural-gas liquefaction and refrigeration of motors, generators, and transmission lines made with high-temperature superconductors, two refrigerators can be joined in series via such a long pulse tube, as illus-

trated schematically in Fig. 1(b). In this arrangement, acoustic power that would previously have been dissipated in the first refrigerator's impedance network is used to drive the second refrigerator, with p_1 and U_1 being optimal in the regenerators of both refrigerators. The number of moving parts is the same as it would be with a single-stage orifice PTR, while the overall energy efficiency can be significantly higher.

II. TUBE DESIGN CONSIDERATIONS

Suppose the designer of a Stirling refrigerator or a PTR takes as given the oscillating pressure amplitude $|p_{1A}|$ and the acoustic power $\dot{E}_A$ at the ambient heat exchanger, as well as the ambient temperature T_A, cold temperature T_C, gas type, mean pressure, and frequency. The designer has freedom to choose the heat-exchanger–regenerator–heat-exchanger geometry and the phase ϕ_A by which U_{1A} leads p_{1A}. (The amplitude of U_{1A} is then determined by $\dot{E}_A = \frac{1}{2}\,|p_{1A}|\,|U_{1A}|\cos\phi_A$.) Best choices for maximizing cooling power and energy efficiency typically yield a phasor diagram similar to that in Fig. 2(a). The pressure amplitude at the cold end of the heat-exchanger–regenerator–heat-exchanger assembly, $|p_{1C}|$, is a little lower than $|p_{1A}|$ because of viscosity. The volume flow rate at the cold end, U_{1C}, is dramatically different from U_{1A}: The part of U_1 that is in phase with p_1 changes by T_C/T_A as the thermodynamics of the refrigeration process consumes acoustic power,[4] and the part of U_1 that is out of phase with p_1 changes because of the nonzero compliance of the intervening components, whose pores necessarily have volume. In particular, best choices yield positive ϕ_A.

Since ϕ_C is negative in Fig. 2(a), connecting a second Stirling refrigerator or PTR to utilize $\dot{E}_C$ does not seem attractive—the second refrigerator's ambient phase would have the wrong sign. Adding a traditional, short pulse tube makes the prospects of connecting an efficient second refrigerator even worse, as shown by the dashed lines in Fig. 2(b), because the compliance of the gas in a traditional pulse tube delays U_1 even further, without appreciably affecting the phase of p_1. However, a long, small-area pulse tube can alter the phases of both p_1 and U_1 so they become optimal for driving a second refrigerator, as shown by the solid curves in Fig. 2(b).

Figures 2(c)-(e) illustrate the basic physics of such a tube in the simplified case of zero temperature gradient and zero viscous and thermal-hysteresis dissipation. In such a tube

with uniform area A, the phasors evolve with axial coordinate x according to

$$p_1(x) \;=\; p_1(0)\cos kx - i\rho a\; u_1(0)\sin kx, \tag{1}$$

$$u_1(x) \;=\; u_1(0)\cos kx - (i/\rho a)\;\; p_1(0)\sin kx, \tag{2}$$

where $u_1 = U_1/A$ is the oscillating velocity, $k = \omega/a$ is the wave vector, ω is the angular frequency, a is the sound speed, and the subscript "1" indicates a complex amplitude with the $e^{i\omega t}$ sign convention throughout this paper. First, consider a pure traveling wave carrying acoustic power in the positive-x direction. Choosing the correct area to maintain such a wave sets $\rho a u_1(0) = p_1(0)$, and both p_1 and u_1 evolve with x as e^{-ikx}. As shown in Fig. 2(c), as x goes from zero to a quarter wavelength, this phasor factor rotates clockwise by 90°—both p_1 and u_1 experience 90° time-phase delays from one end of this quarter-wave tube to the other, while their amplitudes and the phase difference between them remains constant. Next, consider the slightly different situation of Fig. 2(d), in which the wave starts out with pressure and velocity in phase and with $\rho a u_1 > p_1$. A quarter wavelength along the tube, $\cos kx = 0$ and $\sin kx = 1$, so Eqs. (1) and (2) show that the phasors evolve with x as shown in Fig. 2(d), with $|p_1|$ higher at the end of the tube, $|u_1|$ lower, and the phase between them still zero. Thus, for given initial p_1 and U_1, choosing the tube area a little smaller than for Fig. 2(c) makes the tube boost $|p_1|$ while transmitting the acoustic power. Finally, consider the situation of Fig. 2(e), in which u_1 starts out with a little more amplitude *and* a later time phase than a pure traveling wave would have. Examination of Eqs. (1) and (2) shows that the quarter-wave tube boosts $|p_1|$ and changes the sign of ϕ in this case. These two effects are in the right directions to transform the phasors at the cold end of a first heat-exchanger–regenerator–heat-exchanger assembly into phasors that are optimal for driving the ambient end of a second such assembly, recovering from both the phase shift in U_1 caused by the first assembly's compliance and the drop in $|p_1|$ caused by the first assembly's viscous losses. Adjustments of area and length and/or addition of a little compliance at either end of the tube allow fine-tuning of the end-to-end changes as desired.

III. REFRIGERATOR DESIGN

Including the effects of dissipation and of x-dependent temperature on ρ and a in a quarter-wave pulse tube makes the analysis a little more complicated[5] than the description above, but still allows the designer to increase $|p_1|$ and change the sign of ϕ to make them optimal for driving a second PTR with the acoustic power left over from a first-stage PTR. To design hardware resembling Fig. 1(b) to test this concept, we used DeltaEC,[6] choosing a size for our first PTR, adding a long pulse tube with roughly the area and length suggested in the previous section, adding a second PTR, and then optimizing the geometry for maximum calculated cooling power in the two cold heat exchangers. Design choices such as the use of helium at a mean pressure $p_m = 3.1$ MPa, a drive amplitude $|p_1|$ at the first-stage ambient heat exchanger equal to $0.10p_m$, a frequency of 60 Hz, and a cold temperature of 110 Kelvin were inspired by our team's historic interest in small-scale natural-gas liquefaction, and the size of the entire system was set by our cost-saving decision to use an old regenerator from that effort[7] in our first stage. Under design conditions, the predicted first-stage cooling power was 1470 W and the predicted second-stage cooling power was 350 W. The addition of that second-stage cooling power is the performance increase made possible by the use of the long pulse tube: The second stage uses acoustic power that would normally be dissipated in the resistance at the end of the first stage.

Figure 3 shows scale drawings of this experimental two-stage refrigerator. Most dimensional details are given in Table I, where lengths reported are along the acoustic axis (vertical in Fig. 3) and diameters are inside diameters.

The inertance and compliance above the second stage were made of standard-size carbon-steel pipes and semi-ellipsoidal heads, welded together. The resistance valve was an off-the-shelf carbon-steel bellows gate valve, also welded into place.

Each regenerator was a stack of stainless-steel screens, held to its target length with tailstock pressure in a lathe while its diameter was cut to the desired dimension. (The 2nd-stage regenerator was ground with a tool-post grinder; the 1st-stage regenerator had been cut more irregularly many years earlier with a carbide cutting tool.) One layer of 10 wire/inch, 0.8-mm-diam-wire stainless-steel screen on each end of each regenerator was included to give the oscillating gas a space to transition from the tight pores of the fine regenerator screens to the less-finely distributed channels of adjacent heat exchangers. Three-mm-diam

stainless-steel rods, with small washers welded on each end while the regenerators were held to their target lengths, served as rivets to keep each regenerator intact while it was inserted into its stainless-steel housing. Four such rivets were used in the first stage, and two in the second stage as shown in Fig. 4(a). The porosities listed in Table I are based on the final dimensions and weights of the fine-screen parts of the regenerators, and the hydraulic radii r_h listed in the table are calculated from the measured porosities α and the nominal wire diameters d_{wire} of the screens using

$$r_h = d_{\text{wire}}\alpha/4(1-\alpha), \tag{3}$$

as recommended by Organ.[8]

The five cross-flow heat exchangers were made of soldered copper except for their stainless-steel or brass housings. The resulting packages let the refrigerator's working gas oscillate vertically through small rectangular channels between fins while a rectangular array of horizontal 9.5-mm-diam, 0.7-mm-wall copper tubes carried cooling water (in the case of ambient exchangers) or condensing natural gas (in the cold exchangers, notionally; but actual experimental practice with electric heaters is described below). Details are given in Table II. The fabrication of each of the five heat exchangers began with water-jet cutting of rectangular copper fins, whose heights were the "length" Δx of the heat exchanger given in Table I, whose widths (the largest dimension) were slightly larger than the diameter of the heat exchanger, and whose thicknesses were as given in Table II. These fins had holes through which the copper tubes would eventually fit. Copper spacers 0.6 mm thick set the gaps between the fins. Each spacer was 3 mm wider than the copper tubes, had holes for the copper tubes, had a height equal to the height of the heat exchanger, and was cut to a point at each end to help make the transition from the heat exchanger to the adjacent component somewhat streamlined. Assembly began with the spacers dipped in molten paste flux and the fins and spacers stacked up, with temporary aluminum rods through the holes keeping the parts aligned. The entire package was then tightly clamped and all the copper fins were soldered to adjacent spacers, with a minimal amount of tin-based lead-free solder, taking care to block no passages between fins. Removing the aluminum rods yielded a rectangular copper block with small rectangular channels and perpendicular, larger, circular channels. The circular channels were reamed for later insertion of the copper tubes, the block was made round with wire electric-discharge machining, and the package was slipped into its

round pressure-vessel housing (made of stainless steel for the cold heat exchangers, brass for the ambient heat exchangers), as shown in Fig. 4(b). Next, after a little more reaming to fix tiny misalignments between the housing's holes and the holes through the copper block, the copper tubes were inserted, and a rotary tube expander, spun with an electric drill, was used to expand the tubes tightly against the fins and spacers, ensuring good thermal contact. Finally, the copper tubes were sealed to their pressure-vessel housing using lead-tin solder.[9]

The second-stage pulse tube was rather conventional, machined from stainless steel, with the same area as the adjacent heat exchangers to avoid the need for aggressive flow straighteners, and with a length equal to about 18 times the gas peak-to-peak stroke under design conditions. It was not tapered to suppress Rayleigh streaming,[10] because we were more concerned with low fabrication cost than with demonstrating the highest possible efficiency in this stage.

The first-stage pulse tube was a 4.45-m length of schedule-40 seamless stainless-steel pipe, straight for some of the measurements and coiled to form a four-turn helix with a centerline radius of about 15 cm and a pitch of about 12 cm for other measurements. The cross-sectional area and length of the straight tube were accurately known, and are listed in Table I. To form the coiled tube, we made eight 180° bends as close together as possible with a large pipe bender. This crude process resulted in some uncertainty about the internal cross-sectional area and the total length of the coiled tube. We believe that the internal area was 2–3% lower than that of the straight tube, and the lengths differed by no more than 0.5%. Fortunately, the performance of the quarter-wave pulse tube is insensitive to geometrical variations like this.[5]

The transition to turbulence in the boundary layer in oscillating flow in tubes with $D \gg \delta_\nu$ occurs when the ratio $|\langle\xi_1\rangle|/\delta_\nu$ reaches roughly 200, where $|\langle\xi_1\rangle| = |U_1|/\omega A$ is the lateral spatial average of the gas displacement amplitude, δ_ν is the viscous penetration depth, and D is the tube diameter.[11,12] Under design conditions, $|\langle\xi_1\rangle|/\delta_\nu \gg 200$ throughout the long pulse tube. This is dramatically different from the laminar boundary-layer oscillations encountered in traditional pulse tubes. The total length of this tube is 40 times the highest value of $|\langle\xi_1\rangle|$ under design conditions, significantly larger than usual in traditional pulse tubes.

The compliance of the transition cone at the ambient end of the long pulse tube is a

deliberate, significant part of the design, accounting for a 12° phase delay in U_1. However, design calculations showed that minimizing such compliance at the much more severe area transition at the cold end of the tube was vital, so we adopted a novel low-volume, three-part transition. Starting at the top of that transition in Fig. 3(d), a cone 3.3 cm long changed the diameter from that of the long pulse tube at one end to 5.1 cm at the other end. Next came seven tubes, each 1.3 cm diam and 20 cm long, with one straight tube in the center and six bent tubes arrayed around it. The central tube and two of the six surrounding tubes are visible in Fig. 3(d). (The central tube extended farther into the cone above, to keep its length and inertance equal to those of the other six.) At the top, the centerline of each of the six bent tubes was only 1.9 cm from the centerline of the central tube, and the bends in the six tubes increased that distance to 6.0 cm at the bottom. Finally, seven conical bores only 0.5 cm long in the top head of the first-stage cold heat exchanger spread out the flow from the seven tubes to cover 78% of the area of the cold heat exchanger, ending in a 2-mm full-area gap. This entire area transition held only 370 cm^3 of gas while changing the flow area from 9.6 cm^2 to 270 cm^2.

Flow straighteners at the six locations indicated by "FS" in Figs. 3(c) and 3(d) were made of one layer of 10 wire/inch, 0.8-mm-diam-wire stainless-steel screen and three layers of 20 wire/inch, 0.5-mm-diam-wire stainless-steel screen, with the coarser screens abutting the heat exchangers.

The second-stage regenerator, cold heat exchanger, and pulse tube were insulated with many wraps of fiberglass-blanket insulation whose total thickness was several cm. The first-stage ambient heat exchanger, regenerator, cold heat exchanger, and three-part area transition were buried in sub-cm-diam shredded styrofoam (from a bean-bag chair) held in a cardboard box. The long, straight pulse tube was wrapped with strips of fiberglass-blanket insulation to a diameter of about 7 cm, over which was fitted clam-shell, jacketed fiberglass pipe insulation with 6.4 cm i.d. and 11.4 cm o.d. The long, coiled pulse tube was wrapped in foam-rubber insulation along its warmest 0.5 m, and encased in self-expanding insulating foam (Dow Great Stuff) elsewhere.

Variac-powered electric-resistance heaters were inserted in the copper tubes in the cold heat exchangers to load the refrigerators. Six dozen type-K thermocouples[13] were attached throughout the system. In the heat exchangers, 1.5-mm-diam sheathed thermocouples were inserted into drilled holes and soldered in place; elsewhere, thermocouple wires

were spot welded to the outside of stainless-steel components. Eight piezoresistive pressure transducers[14] were also included in the system. Most importantly for the results below, the long pulse tubes, both straight and coiled, had five equally spaced pressure transducers (including two on the end fittings) and ten equally spaced thermocouples (including two on the end fittings).

In operation, temperatures were recorded two or three times per minute by computer. The Variacs controlling the resistance heaters were adjusted by hand to maintain desired cold temperatures, and the driver voltage was adjusted by hand to maintain a desired pressure amplitude below the first-stage ambient heat exchanger, in the middle of the driver assembly. Pressure signals were detected with a lock-in amplifier, whose phase was chosen to be zero at the driver transducer, and recorded by hand when we judged that steady-state temperatures had been reached, after roughly two to five hours of operation at steady amplitude and steady cold temperatures. Temperatures in the middle of the long pulse tube took the longest to reach steady state.

IV. DRIVER DETAILS

We designed this two-stage refrigerator to be driven below the first-stage ambient heat exchanger at 60 Hz with 8 kW of acoustic power at $|p_{1D}|/p_m = 0.10$ in 3.1-MPa helium, but we did not have such a powerful driver. To make partial progress under these limited circumstances, we actually used a 50-50 helium-argon mixture at 2.1 MPa and 27 Hz in the experiments. If the Prandtl number of this mixture were equal to that of pure helium, and if we had chosen the frequency 1 or 2 Hz higher, retaining $|p_{1D}|/p_m = 0.10$, this experimental setup could have been strictly similar[15] to the design conditions: Reynolds and Mach numbers everywhere, wavelength and wave shape, viscous and thermal penetration depths everywhere, and temperatures everywhere would have been exactly the same, with driver power, cooling powers, and ambient heat-rejection powers all scaled down by a factor of $(p_m a)_{50\text{–}50} / (p_m a)_{\text{helium}} = 0.3$. The fact that the Prandtl number of pure helium is 0.7 while that of this mixture is about 0.4 (both approximately independent of temperature)[16] makes the penetration depths mismatched a little, as shown in Table III, and has a similar small effect on Reynolds numbers via the viscosity, but we believe these are still close enough to the design conditions to provide a valid assessment of the utility of the long pulse tube. Another

small compromise, in frequency, arose because the wavelength could not be simultaneously matched in both the second-stage inertance (designed for 300 K, and operated there) and the variable-temperature long pulse tube (designed for $T_C = 110$ K $< T(x) < 300$ K, but operated with $T_C = 200$ K and ~ 140 K).

To drive the system at this reduced power, we combined three small linear-motor units[17] in parallel, with their oscillation axes horizontal and facing toward a common center in a manifold below the first stage, equally spaced at 120° for vibration balance. A 5-kg copper cylinder was bolted to each 10-cm-diam piston face to reduce the resonance frequency appropriately.

Even with the three-fold reduction in driver power resulting from this similitude-based change in gas, we could not reach $T_c = 110$ K and $|p_{1D}|/p_m = 0.10$ with these small drivers, so the results below are for somewhat less demanding operating conditions.[18]

V. RESULTS

With the helium–argon mixture discussed above, with ambient temperatures of 290 ± 6 K (varying from day to day and throughout each day), and with the second-stage resistance valve open 3 turns, we made measurements with the long, straight pulse tube at $T_C \simeq 200$ K at seven drive amplitudes up to $|p_{1D}|/p_m = 0.09$ and at $T_C = 138$ K with $|p_{1D}|/p_m = 0.08$. With the long, coiled pulse tube, we omitted the four lowest-amplitude operating points at 200 K, and took the colder operating point at 144 K because ambient-air temperature was much warmer on that day. We emphasized the straight pulse tube because we are more confident of our ability to model it. In a curved pipe, dp_1/dx is higher along the inside of the curve than along the outside, which might affect the inertance per unit length. The crude fabrication of the coil resulted in uncertainty in its area and length, and the curved geometry also makes it much more difficult to model the insulation around it and heat leak to it.

Assessment of our understanding of the measurements and the refrigeration system relies on comparisons between the measured results and a DeltaEC model of the system, described in the first subsection below. The second subsection focuses on three approaches to understanding the long pulse tube.

A. System-modeling details

We and others have used DeltaEC[6] (and its previous incarnation, DeltaE) for design and analysis of thermoacoustic and pulse-tube systems for almost two decades. DeltaEC numerically integrates one-dimensional energy, momentum, and continuity equations to obtain $T(x)$, $p_1(x)$, and $U_1(x)$ through a series of segments representing the geometry of thermoacoustic hardware. In the built-in mathematics for each segment, lateral dependences of variables such as u_1 are automatically accounted for. Known values of the integration variables, such as temperatures of heat exchangers or pressure amplitudes at transducer locations, can be targeted by DeltaEC's shooting method, with other variables such as heater powers and the initial value $U_1(0)$ adjusted by DeltaEC to hit the targets.

The DeltaEC model[19] for each data set was forced to match the measured heat-exchanger temperatures, letting DeltaEC calculate heater powers at each heat exchanger. DeltaEC was forced to match p_1 in the second-stage compliance, so U_1 at the bottom end of the second-stage compliance was accurately modeled. Agreement with measured p_1 below the resistance valve was enforced, by leaving DeltaEC free to choose a value for the complex impedance of the resistance valve. Leaving DeltaEC free to choose a value for the hydraulic radius in the second-stage regenerator let it target $|p_1|$ at the top end of the long pulse tube. Finally, letting DeltaEC choose the hydraulic radius in the first-stage regenerator let it target the measured $|p_{1D}|$.

Admitting our large uncertainty about the hydraulic radii and valve impedance brings the calculated values of everything into good agreement with the measurements. The reasonableness of DeltaEC's choices for these variables, listed in Table IV, helps establish confidence for subsequent analysis relevant to the long pulse tube. Minor-loss coefficients[20] K are typically around 6 for half-open gate valves, close to the values found by DeltaEC for the real part of the impedance of the resistance valve. DeltaEC consistently found a small, negative value for the imaginary part of the valve impedance, indicated by small negative lengths listed in the table. DeltaEC found consistent values for r_h in each regenerator, except that the first-stage r_h fits seemed to form two well-separated clusters of values, which we do not understand. Finally, a pressure-phase error of 2° to 4° at the drivers is reasonably small after that phase has evolved with x about 160° from the closest place the model's pressure phase is constrained to match the experiment's, below the second-stage resistance valve.

B. The long pulse tube

In the full-system DeltaEC model, the long pulse tube was represented by a series of ten isothermal ducts, each set to a measured temperature, with the midpoints between thermocouples defining the divisions between the ducts, as shown for one case in Fig. 5(a). Defining the model's $T(x)$ accurately (though stepwise) ensured that the temperature dependences of ρ and a were well accounted for in the integrated solutions for $p_1(x)$ and $U_1(x)$, and the use of DeltaEC's isothermal DUCT instead of its x-dependent-temperature STKDUCT allowed turbulence to be included. The calculated acoustic power dissipated in the long pulse tube ranged from 6% to 13% of the acoustic power transmitted along the tube (rising with amplitude), and hence the dissipated power was an equally small fraction of the gross cooling power calculated at the first-stage cold heat exchanger. In a laminar STKDUCT pulse tube, DeltaEC's built-in mathematics would establish a relationship between $\dot{H}$ and $\dot{E}$, where $\dot{H}$ is the total power and $\dot{E}$ is the acoustic power flowing up the tube. In this turbulent tube, we had to arbitrarily choose such a relationship. We decided to set $\dot{H} = \dot{E}$ at the midpoint of the tube, so half of the acoustic-power dissipation in the tube became a load to the first-stage cold heat exchanger. A different choice here would change the calculated cooling power up or down no more than 16%, without changing other results.

Figure 5(b) then shows the typically excellent agreement between the calculated and measured $p_1(x)$'s. The evolution of the phasors in Fig. 5(b) should be compared in detail with that in Fig. 2(e) to appreciate the transformation of the phasors along the quarter-wave tube. In Fig. 5(b), the pressure amplitude dips and rises with x with little net change while its phase decreases by 149°, and $|U_1|$ rises and falls, with a net decrease of 22%, while the phase of U_1 decreases by 60°. Overall, the $p_1 - U_1$ phase difference evolves from +47° to −39° along the tube.

For each operating point, an auxiliary DeltaEC model for the long pulse tube alone yielded a continuous curve for $T(x)$ and incorporated heat leak through its insulation, while ignoring turbulent dissipation of acoustic power. In the auxiliary model, DeltaEC integrated through a series of nine STKDUCTs, with initial conditions at the cold end obtained from the full-system model. At each break between STKDUCTs, at the thermocouple locations, a calculated estimate of the local heat leak was added to the model, changing $\dot{H}$ carried through the next STKDUCT. The geometry of the insulation and handbook values for the

thermal conductivity of fiberglass yield a heat leak through the fiberglass of (0.21 W/m-K)$[T_{\rm room} - T(x)]$, and measurements of $T(x,t)$ while the tube warmed after the drive was shut off at the end of a run suggested that the coefficient was roughly 0.15 ± 0.05 W/m-K. This yielded a $T(x)$ in qualitative agreement with measurements: rising most quickly near $x = 0$, and lying above ambient temperature throughout the warmest third of the tube. Finally, to form a quantitative measure of how much energy was being transported along the tube, we let DeltaEC adjust the tube's perimeter artificially up or down from the actual perimeter, by a multiplier N, thereby artificially increasing or decreasing the calculated boundary-layer energy flow from what it would be in laminar flow, letting DeltaEC minimize the rms temperature difference between the calculated and measured temperatures along the tube. One example of such a calculated temperature profile is shown in Fig. 5(c). If the thermoacoustic energy transport along the tube were powerful enough to overwhelm the heat leak, N would be large and the curve would be straighter; if the thermoacoustic energy transport were shut off, N would be zero and the curve would rise even more abruptly at its cold end. The best N for each data set yielded rms temperature differences between calculations and measurements ranging from 2 to 5 Kelvin, rising with oscillation amplitude and roughly proportional to the value chosen for the fiberglass-heat-leak coefficient.

Figure 6 shows the best N for all of the straight-pulse-tube data sets, plotted against the range of $|\langle \xi_1 \rangle| / \delta_\nu$ along the long pulse tube. Based on these ranges, the boundary layer should be turbulent in all cases. Since N is comparable to 1, the heat transport along the tube is not terribly large. The low values of N at high amplitudes actually suggest that the boundary-layer thermoacoustic energy transport is smaller in turbulent flow than in laminar flow. Analysis of the coiled-tube data with this method was less convincing, because we had no good estimate of the heat leak. Varying both N and the heat-leak parameter to minimize the rms temperature error for each data set yielded broad minima with heat-leak parameters no more than a factor of 2 smaller than the value for the straight tube and with $N \sim 0.5$. (Note: All coiled-tube data had $|\langle \xi_1 \rangle| / \delta_\nu \geq 650$, where the straight-tube data also suggest $N \sim 0.5$).

The good agreement between measured and calculated first-stage cooling power shown in the upper parts of Figs. 7(a) and 7(b) is additional evidence that the energy transport down the long pulse tube is not anomalously large, whether it is straight or coiled.

Agreement for the second stage, which has a traditional pulse tube, is not as good.

Calculations suggest that Rayleigh streaming[10] in that pulse tube, from ambient to cold in the outer part of the tube, could be loading the second-stage cold heat exchanger. Consistent with that explanation, the thermocouples spot-welded along the wall of the second-stage pulse tube showed a non-linear $T(x)$, with the center temperature greater than the average of the two end temperatures, and quickly becoming more nearly linear as soon as the acoustic oscillations were shut off.

The slow evolution of $T(x,t)$ in the long pulse tube toward its steady-state profile when the refrigerator was first turned on also supports the claim that turbulent energy transport along the tube is not anomalously large. For two of the data sets (one straight; one coiled) with $T_C = 200$ K and intermediate $|p_{1D}|/p_m$, we drove the refrigerator at the highest possible $|p_{1D}|/p_m$ for ~ 0.5 hr to cool the first-stage cold heat exchanger to 200 K as quickly as possible, and then reduced the drive to maintain 200 K $\pm$ 5 K during the subsequent 4 hr, recording $T(x,t)$. In an idealized heat-conduction situation with an initial condition of $T(x,0) = 300$ K and boundary conditions of $T(0,t) = 200$ K and $T(L,t) = 300$ K, the time evolution of the temperature would be given by[21]

$$T(x,t) = (200\text{ K}) + (100\text{ K})\,\frac{x}{L} + \sum_1^\infty a_n \sin\frac{n\pi x}{L} e^{-\kappa n^2\pi^2 t/L^2}, \tag{4}$$

where the a_n are coefficients given in the reference and κ is the axial thermal diffusivity. We modeled κ as laminar boundary-layer thermoacoustic heat transport times the multiplier N. At mid-tube, the $n = 1$ term in Eq. (4) is the largest and the even-numbered terms are zero. For the straight tube, fitting a simple exponential to the data at mid-tube yielded a time constant of 3 hr, implying $N = 1$; for the coiled tube, the fit yielded $N = 1.3$. At the quarter-tube location, the $n = 2$ term in Eq. (4) is the largest. Fitting a simple exponential to that thermocouple's data in the straight tube yielded a time constant of 1.4 hr, implying $N = 0.6$; for the coiled tube, the fit yielded $N = 0.8$. These values are roughly equal to those obtained in Fig. 6.

VI. SUMMARY AND FURTHER DISCUSSION

A long pulse tube can transform the pressure and volume flow rate phasors at the exit of one refrigeration stage's cold heat exchanger into phasors suitable for driving a second stage of refrigeration. To do so, the area of the long pulse tube must be small. The small area

forces the oscillating velocity in the tube to be high, resulting in a turbulent boundary layer. Despite the general rule that turbulence increases heat transfer, three lines of experimental evidence suggest that the turbulence in such a long pulse tube does not impose a high heat load on the first stage. First, the shape of $T(x)$ in steady state is consistent with low heat transport down the tube. Second, the measured first-stage cooling power shows no sign of high heat load from the tube. Third, the initial cooldown of the tube is reasonably slow, suggesting that the middle of the tube is not tightly coupled to its ends. Apparently, the turbulence in this tube neither enhances the boundary-layer thermoacoustic heat transport above its laminar value[22] (perhaps even reducing it) nor significantly increases the axial conduction of the gas via turbulent eddies.

Coiling the tube brings additional physics into play that one might have imagined would increase the end-to-end heat transfer in the tube, yet the experiments showed no such increase. Regimes of oscillating flow in a curved tube are spanned by three dimensionless variables, often[23] taken to be R/r (where R is coil radius and r is tube radius), the Womersley number $\sqrt{2}r/\delta_\nu$ (where δ_ν is viscous penetration depth), and the Dean number $N_{R1}\sqrt{r/R}$ (where N_{R1} is the amplitude of the Reynolds number of the oscillating flow). In the modest-R/r, high-Womersley, high-Dean limit where this tube operates, a vigorous secondary flow known as Lyne circulation[24] appears in the cross section of the tube. This circulation consists of four steady vortices, two of which are flattened against the walls while the other two fill most of the cross section. The circulation velocity is much faster than the oscillating velocity.[23] Perhaps this rapid transverse circulation keeps each cross section spatially isothermal at each instant of time, preventing the transversely nonuniform oscillating axial velocity (highest near the inside of the coil, lowest near the outside) from causing large axial heat transport.

We expect the quarter-wave pulse tube idea to work best for high-power refrigerators. The acoustic-power dissipation in a tube is proportional to perimeter while the useful power that can be transmitted is proportional to cross-sectional area, so the long, narrow tubes that might otherwise seem suitable for low-power refrigerators would tend to dissipate too much acoustic power.

The acoustic power available for recovery after a cold heat exchanger is, at most, T_C/T_0 times the acoustic power driving that refrigerator.[4] Thus, for the purpose of feeding such acoustic power to a second stage, the most useful applications would be those with T_C/T_0

not too small, such as natural-gas liquefaction where $T_c \geq 110$ K. However, based on the evidence here showing that the boundary-layer heat transport down the long tube is very small and there is no indication of heat carried by Rayleigh streaming, this concept may be useful simply for reducing the heat load on a refrigerator's cold heat exchanger at very low T_C, even if the recovery of the acoustic power does not seem worthwhile.

Acknowledgments

This work was supported by the Technology Transfer Division at Los Alamos National Laboratory.

---

[1] R. Radebaugh. Development of the pulse tube refrigerator as an efficient and reliable cryocooler. *Proc. Institute of Refrigeration (London)*, pages 11–29, 2000. http://cryogenics.nist.gov/Papers/Institute_of_Refrig.pdf.

[2] G. W. Swift. *Thermoacoustics: A Unifying Perspective for some Engines and Refrigerators*. Acoustical Society of America Publications, Sewickley PA, 2002.

[3] K. M. Godshalk, C. Jin, Y. K. Kwong, E. L. Hershberg, G. W. Swift, and R. Radebaugh. Characterization of 350 Hz thermoacoustic driven orifice pulse tube refrigerator with measurements of the phase of the mass flow and pressure. *Adv. Cryogenic Eng.*, 41:1411–1418, 1996.

[4] P. Kittel. Ideal orifice pulse tube refrigerator performance. *Cryogenics*, 32:843–844, 1992.

[5] Scott Backhaus and Greg Swift. Thermoacoustic refrigerators and engines comprising cascading Stirling thermodynamic units, 2009. US Patent Application 20090249797.

[6] Bill Ward, John Clark, and Greg Swift. Design Environment for Low-amplitude Thermoacoustic Energy Conversion (DeltaEC), version 6.2, 2009. Software and User's Guide available from the Los Alamos thermoacoustics web site www.lanl.gov/thermoacoustics/. Some examples of code validation are given in the User's Guide.

[7] G. W. Swift, M. S. Allen, and J. J. Wollan. Performance of a tapered pulse tube. In R. G. Ross Jr., editor, *Cryocoolers 10*, pages 315–320. Plenum, New York, 1999.

[8] A. J. Organ. *Thermodynamics and Gas Dynamics of the Stirling Cycle Machine*. Cambridge University Press, 1992.

[9] A few of these tube-to-housing joints in the first-stage cold heat exchanger began leaking during the first cooldown of the refrigerator. We believe this occurred because the tube-expansion assembly step closed the small gap between the tubes and their holes through the pressure housing, preventing solder from wicking in to make a reliable seal. If we were to assemble heat exchangers like this again, we would switch the order of the last two steps, soldering the tubes to the housing before expanding the tubes, with the holes through the housing pre-tinned.

[10] J. R. Olson and G. W. Swift. Acoustic streaming in pulse tube refrigerators: Tapered pulse tubes. *Cryogenics*, 37:769–776, 1997.

[11] P. Merkli and H. Thomann. Transition to turbulence in oscillating pipe flow. *J. Fluid Mech.*, 68:567–579, 1975. and references therein.

[12] M. Ohmi, M. Iguchi, K. Kakehashi, and M. Tetsuya. Transition to turbulence and velocity distribution in an oscillating pipe flow. *Bull. JSME*, 25:365–371, 1982.

[13] Type K thermocouples, standard limits of error (2.2°C), Omega Engineering, Stamford CT, www.omega.com, detected and recorded via a personal computer using Labview, National Instruments, Austin TX, www.ni.com.

[14] Model 8510B-500 (500 psi full scale), Endevco, San Juan Capistrano, CA, www.endevco.com. Manufacturer specifies 500 kHz resonance frequency and 0.5% of full scale maximum error. Our cross calibrations among transducers and with a calibrated Bourdon-tube gauge suggest that the actual errors are less than half of this. Detected via Model SR830 lock-in amplifier, Stanford Research Systems, Sunnyvale CA, www.srsys.com

[15] J. R. Olson and G. W. Swift. Similitude in thermoacoustics. *J. Acoust. Soc. Am.*, 95:1405–1412, 1994. See discussion of "pressure–gas scaling."

[16] F. W. Giacobbe, "Estimation of Prandtl numbers in binary mixtures of helium and other noble gases," J. Acoust. Soc. Am. 96:3568–3580 (1994).

[17] Model C2 (similar to the newer STAR-1S241D), Chart-QDrive, Troy NY, http://qdrive.com.

[18] In general, neon would have been a better choice than 50–50 helium–argon for these reduced-power similitude-matched experiments, because its Prandtl number more closely matches that of helium, and because 2.3-MPa neon remains a gas at 110 K while argon at a partial pressure of 1 MPa condenses at 120 K. However, our existing drivers would have gotten the refrigerator no colder with neon than with the helium–argon mixture.

[19] A typical model set, matched to one of the operating conditions described here, is available at

www.lanl.gov/thermoacoustics/Pubs/He-Ar1222c.out and .../He-Ar1222cTbtCone.out.

[20] V. L. Streeter. *Handbook of Fluid Dynamics*. McGraw-Hill, 1961.

[21] H. S. Carslaw and J. C. Jaeger. *Conduction of Heat in Solids*. Oxford University Press, second edition, 1959, Sec. 3.4.

[22] Ref. 2, Eq. (5.29).

[23] K. Sudo, M. Sumida, and R. Yamane. Secondary motion of fully developed oscillatory flow in a curved pipe. *J. Fluid Mech.*, 237:189–208, 1992.

[24] W. H. Lyne. Unsteady viscous flow in a curved pipe. *J. Fluid Mech.*, 45:13–31, 1970.

Table I. Some key dimensions and other details of the two-stage refrigerator. HX = heat exchanger. Poros = volumetric porosity. The compliance had semi-ellipsoidal heads on each end, so its "length" in this table is its volume divided by the cross-sectional area of its central, straight portion. Conical transitions in area on the ends of the second stage are indicated by an end-to-end range in diameters. The more complicated transition in area between the long pulse tube and the first stage is described in the text. Hydraulic-radius transitions and flow straighteners between the listed components, comprising one or a few layers of coarse-mesh screen, are described in the text.

	Δx(cm)	D(cm)	Poros.	r_h(μm)
Second stage:				
Compliance	26.8	20.6		
Transition	10.1	5.64–2.43		
Inertance	185	2.43		
Resistance		$\leq$1.8		
Transition	8.6	1.8–9.44		
Top ambient HX	1.5	9.44	0.129	300
Pulse tube	20.0	9.44		
Cold HX	3.1	9.44	0.129	300
Regenerator	5.5	9.44	0.70	18.1
Ambient HX	6.8	9.44	0.156	300
Transition	8.5	9.44–3.5		
Long pulse tube	445	3.5		
Transition	Three-part; see text			
First stage:				
Cold HX	3.0	18.5	0.153	300
Regenerator	5.1	18.5	0.68	18.9
Ambient HX	6.8	18.5	0.138	300

Table II. Number of rows and number of columns of cross-flow tubes, and fin thickness, in each heat exchanger.

	Rows	Columns	Thickness
Second stage:			
Top ambient	1	3	2.0 mm
Cold	1	3	2.0 mm
Ambient	3	3	1.6 mm
First stage:			
Cold	2	5	2.0 mm
Ambient	3	7	1.6 mm

Table III. Comparison of some key variables under design conditions and experimental conditions. Above the central line, choices for establishing near similarity. Below the line, similarity comparisons.

	Design	Experiment
Gas	Helium	50–50 He–Ar
p_m	3.1 MPa	2.1 MPa
Frequency	60 Hz	27 Hz
λ at 300 K	17 m	16 m
δ_κ at 300 K	0.18 mm	0.19 mm
δ_ν at 300 K	0.15 mm	0.12 mm
λ at 150 K	12 m	11 m
δ_κ at 150 K	0.10 mm	0.11 mm
δ_ν at 150 K	0.08 mm	0.07 mm

Table IV. Some DeltaEC choices needed to hit measured targets, for all straight-tube data sets. The two sets at the same pressure amplitude were taken on different days, to check reproducibility. Screen specifications, measurements, and Eq. (3) gave $r_h = 18.1$ and 18.9 μm for the second- and first-stage regenerators, respectively, and the measured phase of p_{1D} was 0° for all measurements. The underlined value seems anomalous, perhaps indicating human error recording a measurement. For the coiled-tube data sets, the results were similar, except that all of DeltaEC's choices for first-stage r_h were below 16 μm, averaging 14 μm.

	Valve K	Valve "Δx"	r_h(stg 2)	r_h(stg 1)	Phase[p_{1D}]
T_C= 200 K:					
$\lvert p_1\rvert / p_m$					
0.029	6.5	−22 cm	24.4 μm	16.3 μm	−2.1°
0.044	6.4	−19 cm	23.8 μm	16.1 μm	−2.0°
0.044	6.5	−14 cm	23.5 μm	13.8 μm	−3.5°
0.053	6.4	−18 cm	23.9 μm	16.7 μm	−2.0°
0.062	6.2	−17 cm	24.0 μm	16.6 μm	−2.2°
0.069	6.2	−16 cm	24.3 μm	17.1 μm	−2.4°
0.080	6.2	−10 cm	24.2 μm	16.0 μm	−4.1°
0.089	6.2	−9 cm	24.7 μm	16.9 μm	−4.3°
T_C= 138 K:					
$\lvert p_1\rvert / p_m$					
0.081	<u>1.8</u>	−12 cm	23.6 μm	13.3 μm	−4.5°

Figure captions

Figure 1. (a) A traditional pulse-tube refrigerator, whose pulse tube is much shorter than a quarter wavelength and has negligible inertance. (b) Replacing that short pulse tube with a quarter-wave pulse tube allows efficient use of a second-stage pulse-tube refrigerator in place of the dissipative acoustic network of (a).

Figure 2. Illustrative phasor diagrams of pressure p_1 and volume flow rate U_1, with the $e^{i\omega t}$ sign convention. Real parts on horizontal axis, imaginary parts on vertical axis. In (b)–(e), normalizations are omitted. (a) Regenerator performance is best when the phases of the pressure phasors fall somewhere between the phases of the volume-flow-rate phasors at the ends of the regenerator. The amplitudes are typically $|p_1|/p_m \sim 0.1$. (b) The dashed lines show how a traditional, short pulse tube exacerbates the phase lag of U_1 relative to p_1 at the cold end of the regenerator. The solid lines show how a long, narrow pulse tube can shift the time phase of p_1 more than that of U_1, optimizing the complex impedance $p_{1\mathrm{longPT}}/U_{1\mathrm{longPT}}$ for use in a second pulse-tube refrigerator. (c) An isothermal quarter-wave tube time-delays a pure traveling wave without affecting its impedance. (d) Selecting the tube area so the velocity is higher than that of a pure traveling wave causes the quarter-wave tube to boost the pressure amplitude. (e) If u_1 lags p_1 at one end of such a tube, it will lead at the other end.

Figure 3. Scale drawings of the two-stage refrigerator. (a) Cross section of the entire apparatus, above the drivers. (b) Coiled version of the long pulse tube, at the same scale as in (a). (c) Cross-sectional close-up of the second stage. (d) Cross-sectional close-up of the first stage. HX = heat exchanger; FS = flow straightener; P = pressure sensor; T = thermocouple temperature sensor. Pore sizes in regenerators and heat exchangers were actually much smaller than indicated by the line spacings in these drawings.

Figure 4. Photos of two typical components of the refrigerator. (a) Second-stage regenerator after diametral grinding. The 10 wire/inch end screen and two rivet heads are visible on top. (b) Second-stage ambient heat exchanger being slipped into its housing.

Figure 5. Numerical results (lines) and measurements (symbols) in the long straight pulse tube, for $T_C = 202$ K, $T_A = 294$ K, and $|p_{1D}|/p_m = 0.080$. We define $x = 0$ at the bottom of the flow straightener below the first-stage ambient heat exchanger. (a) In the full-system numerical model, the long pulse tube was treated as a series of isothermal ducts at measured

temperatures. (b) Phasors in the long pulse tube. The calculation forces equality in $|p_1|$ at $x = 4.9$ m, but all other points on the curves are calculated from the momentum and continuity equations, with the other three end conditions at $x = 4.9$ m established by the integrations through the second-stage refrigerator. Note the end-to-end change in phase of p_1 by $> 90°$ and in phase of U_1 by $< 90°$, as shown in Fig. 2(e). (c) In the auxiliary numerical model, an estimate of heat leak was injected at ten locations (one of which is visible as a kink near $x = 0.9$ m here). The temperature profile was then calculated with one adjustable parameter to minimize the rms difference between calculated and measured temperatures. The measured temperature closest to the cold end, indicated with the filled circle, was not included in the minimization because it was mounted on a larger-diameter flange and had different insulation than the others.

Figure 6. Ratio N of DeltaEC's best choice of enthalpy transport down the straight pulse tube to the calculated value for a laminar boundary layer, as a function of $|\langle\xi_1\rangle|/\delta_\nu$ in the long pulse tube, for a fiberglass-heat-leak parameter of 0.21 W/m-K. Horizontal bars show end-to-end ranges of $|\langle\xi_1\rangle|/\delta_\nu$; the cold end has the highest values.

Figure 7. Experimental cooling powers (open symbols) and calculated cooling powers (closed symbols) as a function of the square of the drive amplitude. (a) Straight pulse tube. (b) Coiled pulse tube. Heat leak from room air to the cold heat exchangers, which was not taken into account, could be responsible for the amplitude-independent parts of the differences between calculated and experimental values.

Figure 1

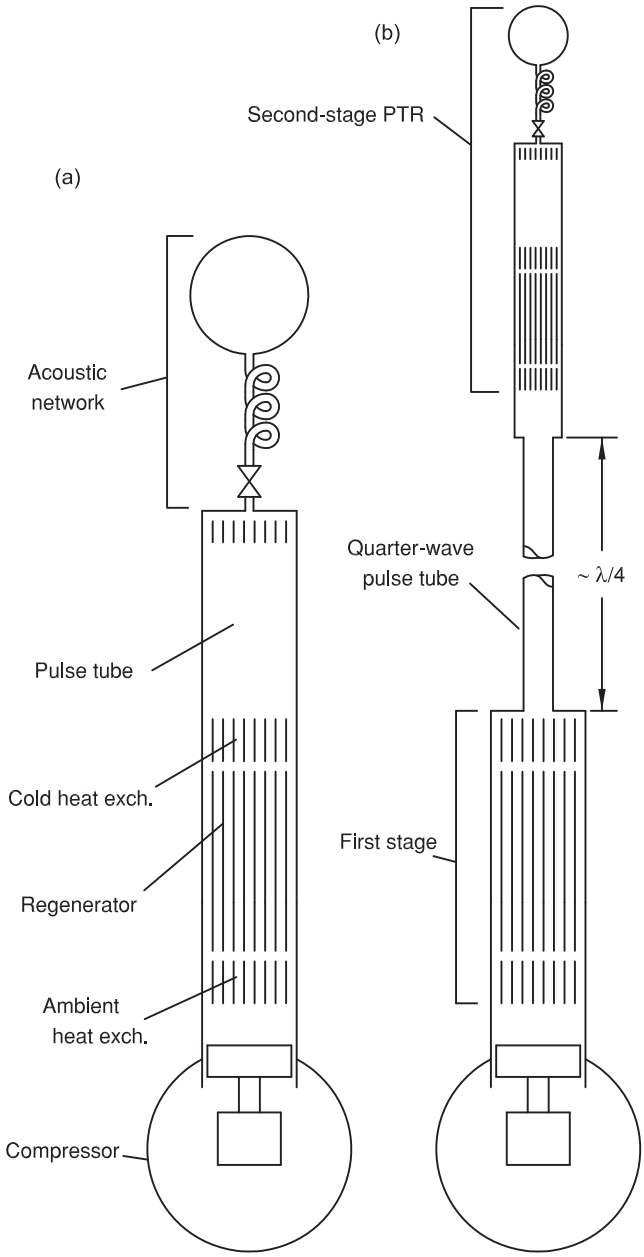

Figure 1
Swift, Gardner, and Backhaus
Cryogenics

Figure 2

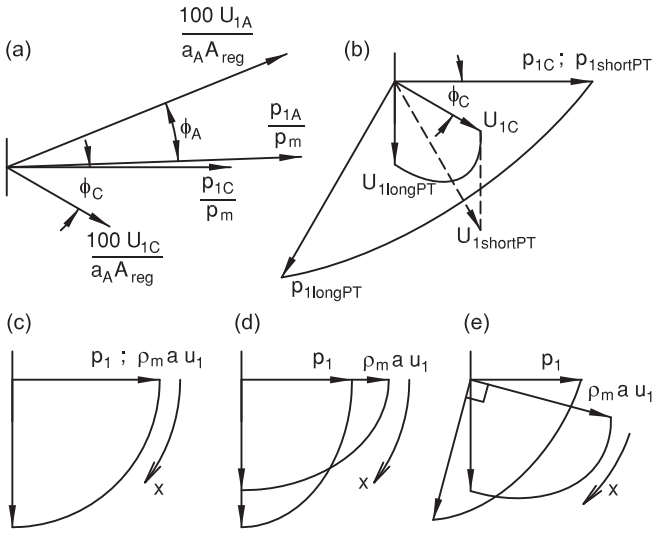

Figure 2
Swift, Gardner, and Backhaus
Cryogenics

Figure 3

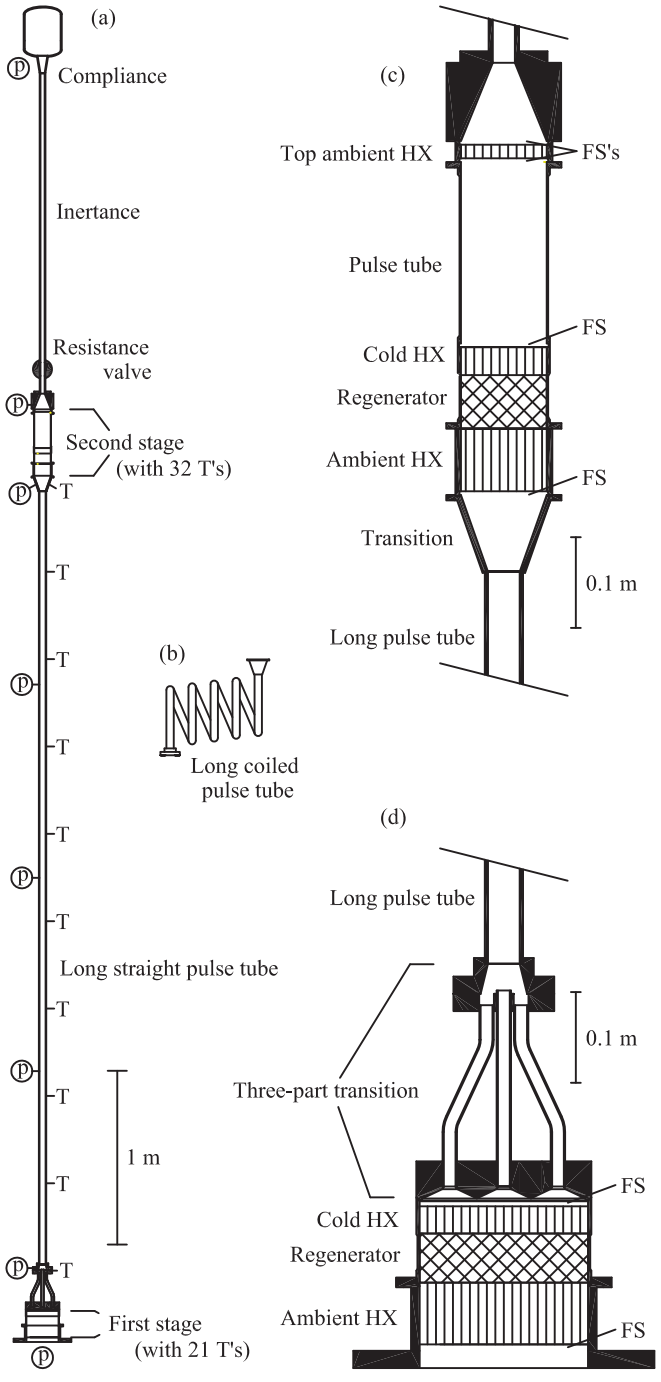

Figure 3
Swift, Gardner, and Backhaus
Cryogenics

Figure 4

Click here to download high resolution image

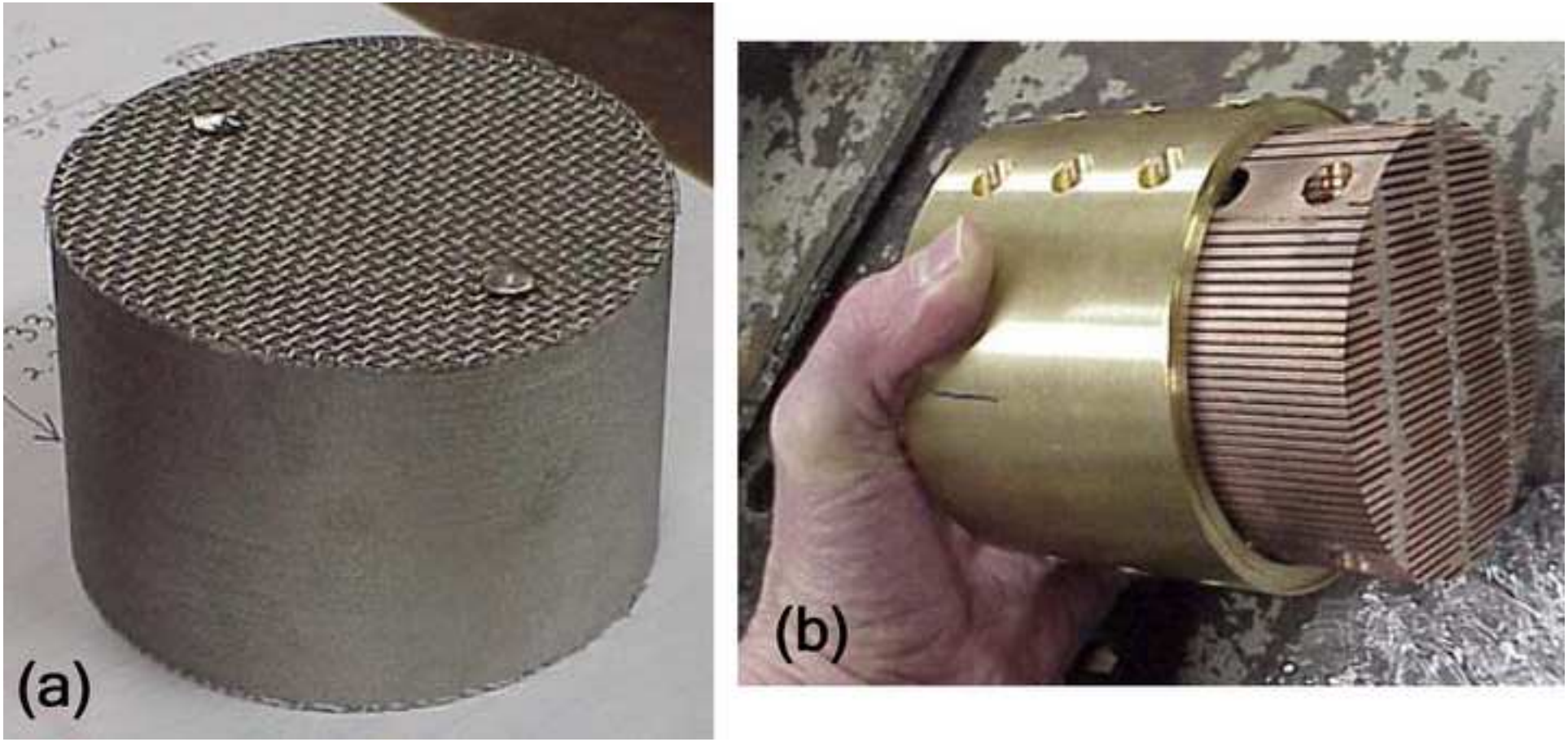

Figure 5

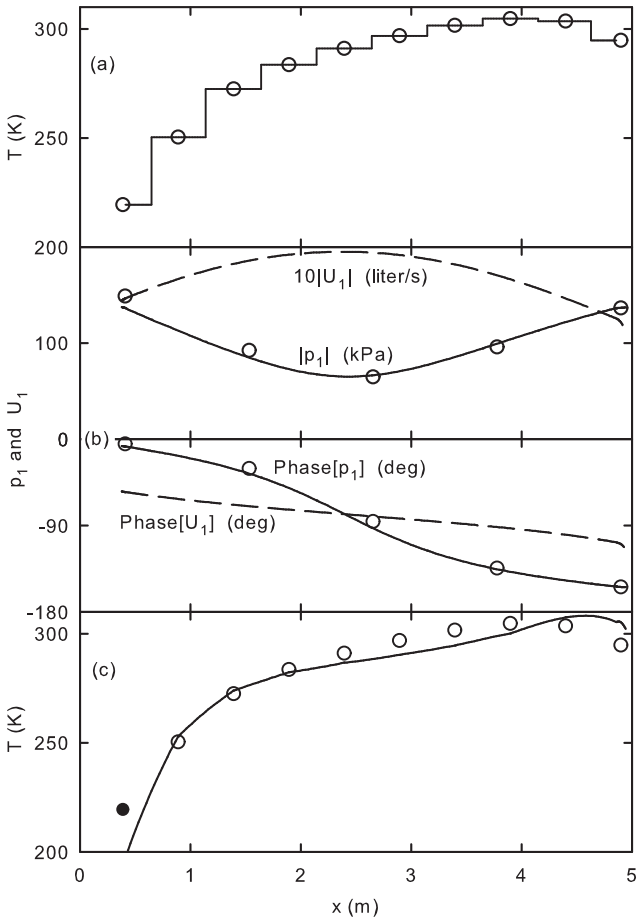

Figure 5
Swift, Gardner. and Backhaus
Cryogenics

Figure 6

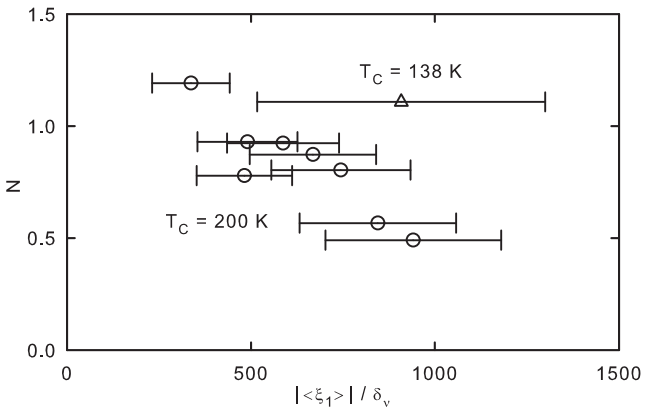

Figure 6
Swift, Gardner. and Backhaus
Cryogenics

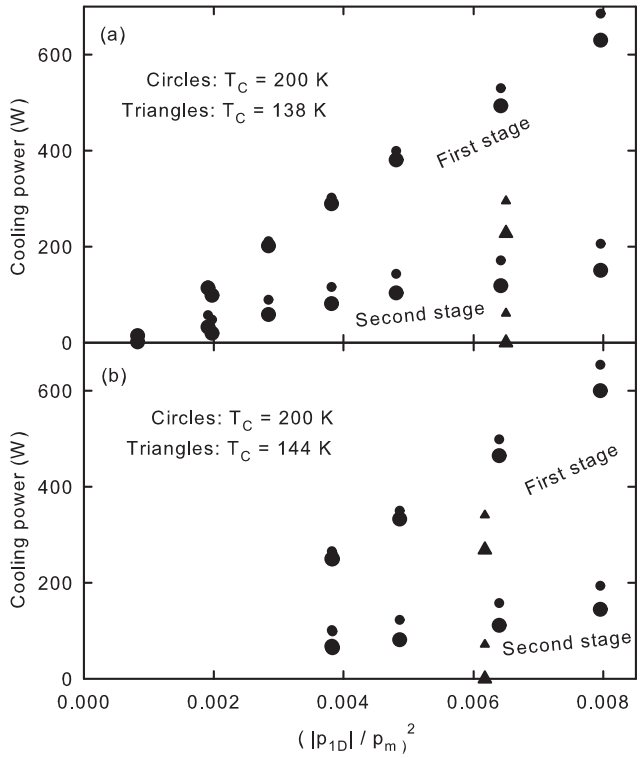

Figure 7
Swift, Gardner. and Backhaus
Cryogenics